An Analytical Method of Evaluating Nonuniformities in Shock Tube Flows. Part 1: Theory and Development.

Matthew Satchell *, Matthew McGilvray †, and Luca Di Mare ‡
Osney Thermofluids Institute, University of Oxford, United Kingdom

Shock tube experiments are a cornerstone of investigations into the hypersonic flight environment. However, the actual flow through the basic shock tube has not been well characterised in the literature, and nonuniformities arising in the test gases are not well understood. This work produces a quasi-one-dimensional analytical methodology for predicting the nonuniformities in the post-shock test gas based exclusively on the experimentally measured history of shock speed down the tube. Wave effects extracted from shock speed variations are shown to provide all information necessary in order to reconstruct the test slug from any particular experiment. Accurate representation of flow dynamics is initially checked against Argon test cases following accelerating and decelerating shock trajectories, each with a tube-end Mach number of 6.5 and a fill pressure of 66.66 Pa in a tube of 100 mm diameter. Agreement between the method and results from a viscous, axisymmetric Navier-Stokes solution is found to within 1% in pressure and temperature.

I. Nomenclature

Variables

U	=	Gas State Variables
p	=	Pressure, Pa
ρ	=	Density, kg/m^3
T	=	Temperature, K
h	=	Static Enthalpy, J/Kg
H	=	Total Enthalpy, J/Kg
u	=	Axial Velocity, m/s
c	=	Sound Speed, m/s
S	=	Flow Area, m^2
r	=	Radius, m

*DPhil Candidate, Department of Engineering Science, Oxford Thermofluids Institute, University of Oxford.
†Associate Professor, Oxford Thermofluids Institute, Department of Engineering Science, University of Oxford.
‡Associate Professor, Oxford Thermofluids Institute, Department of Engineering Science, University of Oxford.

t = Current Time Level, s

t^+ = Future Time Level, s

t^- = Earlier Time Level, s

t^0 = Slice Starting Time Level, s

λ = Wave Speed, m/s

s = Entropy, $J/(KgK)$

l = Distance Between Slice and Shock, m

ω = Characteristics

M = Mach Number

$a_{L/R}$ = Wave Amplification Factor

β = Boundary Layer Shape Factor

C_M^α = Mirels Shape Adjustment Factor

δ = Arbitrary Change in Time or Space

Δ = Change Between Discrete States

γ = Ratio of Specific Heats

Subscripts

$1, 2$ = Pre/Post-Shock States

a, b, c = Post-Shock Time States

sh = Post-Shock Properties

E = Slice Properties

L, R = Riemann Problem States

w = Wall Properties

$\tilde{\cdot}$ = Roe-Averaged Values

δ_m = Mass flow thickness

II. Introduction

Shock tube experiments are vital to the study of the hypersonic environment and provide a unique ground testing source of "clean" thermochemical and radiative data about the flows which are encountered during high speed atmospheric flight. The shock speed is typically set to represent vehicle flight speed and the fill density and composition to that seen at a particular planetary body's altitude point. This experimental methodology allows for the non-equilibrium thermochemistry and radiative absorption/emission behind a shock to be studied as a function of distance/time. As

shown schematically in Figure 1, shock tubes operate by building up pressure in the driver gas (4) behind a diaphragm until it bursts, sending a shock wave through the low pressure test gas at ambient temperature (1). This shock impulsively elevates the temperature, pressure and velocity of the test gas behind it (2), producing conditions representative of those found on the stagnation line of a hypersonic vehicle. The shocked test gas is limited in length/time to the arrival of the expanded driver gas (3), separated by the contact discontinuity (CD).

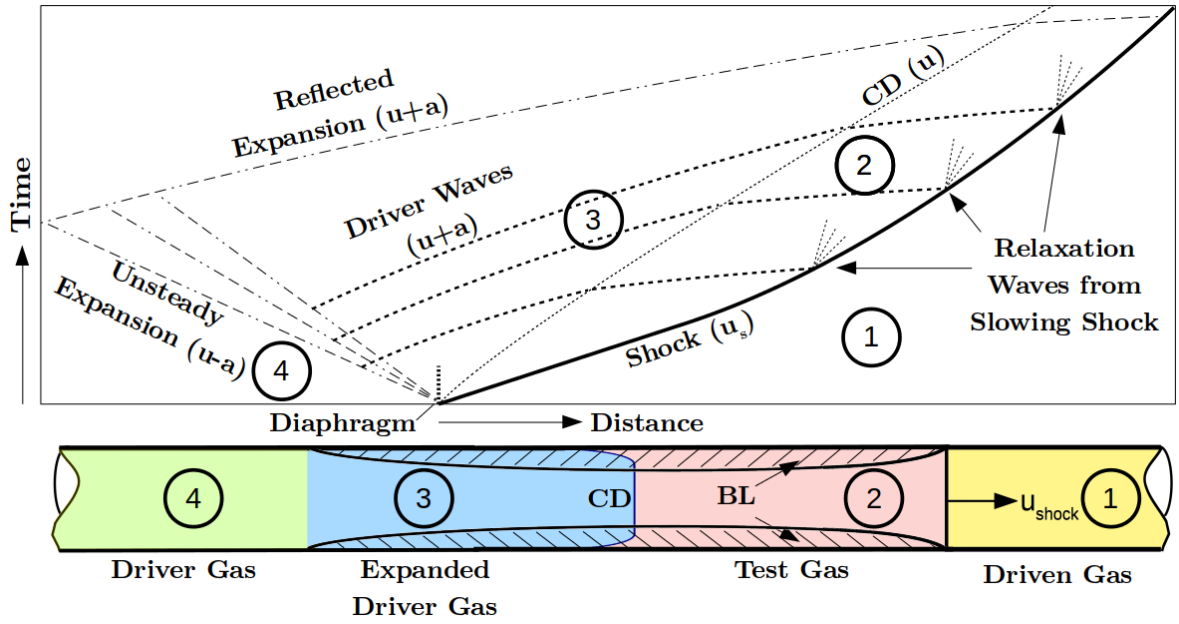

Fig. 1 Distance-time diagram of the primary waves produced by a shock tube (not to scale).

Although shock tubes are seen to have a relatively simple operation, complexity is inherent experimentally which alters the shocks speed down the tube. Several sources produce compression and expansion waves which can reach and alter the speed of the shock wave. Boundary layer (BL) growth along the entire length of the tube, including within the driver gas, produces waves which cause shock attenuation [1]. The driver also causes further waves to reach the shock. This is due to having a finite driver section length, change in volume if a free piston driver is used or transient heating processes if a deflagration, detonation or arc heating driver are used [2]. Additionally, the diaphragm rupture is not an instantaneous process and can introduce a rapid acceleration of the shock and subsequent deceleration, substantially influencing shock tube performance [3, 4]. Thermochemistry also plays a role in the variation of shock speed [5, 6].

Shock speed variation down the tube has a direct effect on the measured test gas behind the shock, as the compressed slices of gas behind the shock will have been processed by different shock speeds [7]. How the properties (speed, pressure temperature, thermochemical state) of any slice of shocked test gas alters as it convects down the tube will be influenced by the shock speed profile. Shock speed variations can be significant. For example, the shock speed in NASA EAST experiments detailed in [8] begin near 12 km/s but reach the end of the tube at 9 km/s. Additionally, there are other effects caused by boundary layer growth in the shocked test gas, namely "Mirels effects" [9]. Behind a

shock of constant speed, the mass lost to the boundary layer causes the gas behind the shock to accelerate in the lab frame of reference towards the shock speed, as seen in Figure 2. This means that as the shocked test gas slices convect downstream that they will cluster towards the contact surface. This effect was shown in Satchell *et al.* [10] to be present also behind shocks undergoing acceleration or deceleration. It should also be noted that gas within the boundary layer will influence any absorption or emission measurements as these are integrated across the diameter of the tube.

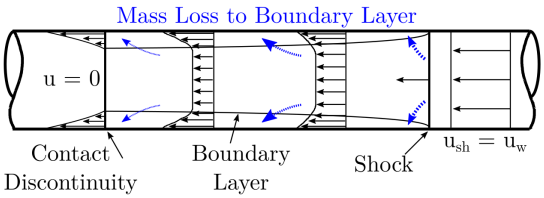

Fig. 2 Core flow acceleration due to mass loss to the boundary layer in the shock frame of reference, adapted from Mirels [1].

Most analysis of the non-equilibrium experimental data from shock tubes simply use the shock speed at the test section or measurement location and the fill conditions. A common analysis is to numerically model a one-dimensional steady state behind a shock of constant velocity using non-equilibrium thermochemistry models [11, 12]. A similar method may be performed to characterize the stagnation-line flow on a large blunt body as an analogy to the post-shock flow, which is a method currently employed by the group at NASA Ames [13]. Many researchers have performed full facility simulations of the shock tube to try to incorporate the more complex effects of driver and boundary layer growth, the simplest being one-dimensional models, such as L1d by Jacobs et al. [14, 15] and Sharma et al. [16], which have simplified models of the boundary layer growth that alter the shock speed and gas slice locations. Simulation complexity may be expanded up to fully two-dimensional simulations of the entire facility, incorporating numerical models of the transient driver and diaphragm opening, which account for the larger proportion of shock speed variation effects [17, 18]. These have the benefit of also calculating the properties within the boundary layer and other multidimensional phenomena. Improved accuracy has been recently introduced by using formulations in the shock frame of reference and overset meshing [4, 5] to ease mesh requirements. These struggle to match the shock speed profiles observed in the physical machine due to simplifications in the numerical models for the drivers and diaphragm ruptures. Additionally, none of the methods described above account for the test to test variations often seen in the shock speed profile and therefore introduce significant additional uncertainties when compared against experimental data.

Mirels [1] and Holbeche [19] sought to develop analytical models of the test gas. Mirels assumed a steady shock speed and used boundary layer theory to develop a simple model to predict the change in gas properties with distance due to the loss of mass flow. Holbeche observed that the relaxation of pressure waves behind a shock of variable strength influences the temperature of the gasses in the test slug, and developed a more complex model which accommodated a variable shock speed, but the method was limited in numerous ways by the assumption of only small variations

in shock speed. Holbeche noted that, due to the short test times, entropy-producing processes such as viscous loss or conduction are insignificant for any element of gas. Light [20] later described the test slug behind a decelerating shock as a series of gas elements processed at different shock strengths which were gradually consumed by boundary layer mass consumption. He then composed a method of obtaining variations in element density and speed based on continuity in a shock-steady frame of reference. However, Light's method assumed small perturbations both in shock speed and properties behind the shock, applying the method only to a small range of conditions, and Light himself acknowledged the limited extent of the application. Importantly, Light comments on how the gas behind a decelerating shock is undergoing constant expansion due to the diminishing shock strength, specifically highlighting the importance of accounting for this effect in future studies.

This paper, the first in a series of two, proposes a new methodology to reconstruct the resulting non-uniform test slug directly taking the experimentally measured shock passing times at several axial positions and the tube fill conditions. The methodology assumes the gas is either a perfect gas or at thermochemical equilibrium. Results from an implementation of this methodology are then verified by comparison to the perfect gas simulations of Satchell *et al.* [10]. The second paper in the series [21] shows the application of the methodology to experiments from the Oxford T6 Stalker shock tube facility [22] in order to demonstrate the generality of the method.

III. Development of a Quasi One-Dimensional Model

Knowledge of the spatial variation of flow velocity, enthalpy and pressure behind the shock is crucial to understand shock tube experiments. These can vary significantly away from current theory due to non-ideal effects and the resulting variations in shock speed. The following methodology characterises the core flow of the shocked test gas in an individual shock tube experiment, by calculating the entropy in each portion of the test gas and then determining its enthalpy. This calculation takes the shock speed trajectory and initial test gas fill conditions as inputs, and from that efficiently predicts the thermodynamic properties of the entire test slug. It accounts for the Mirels effects (*i.e.* boundary layer mass loss) within the calculation, though does not directly calculate the properties within the boundary layer. Overall, this gives a quasi one-dimensional representation of the experiment. This methodology is validated herein against data from the FROSST solver [4], and more extensively against experimental data in a follow-on paper [21].

For a perfect gas, Satchell *et al.* [10], showed the only influence on the entropy of an individual gas packet is the shock speed that processed it. This observation should hold for a gas in thermochemical equilibrium. Assuming that gas outside the boundary layer at a given axial distance from the shock may be treated as radially homogeneous, the observation of isentropic gas packets may be applied to the slices described above, and obtaining the enthalpy becomes a matter of performing an energy balance. This observation constitutes the basis of the following analysis.

The test slug of a shock tube experiment is comprised of initially stationary gas which is processed by the shock and then moves at a slower rate than the shock, causing the gases to propagate away from the shock, with the interstitial

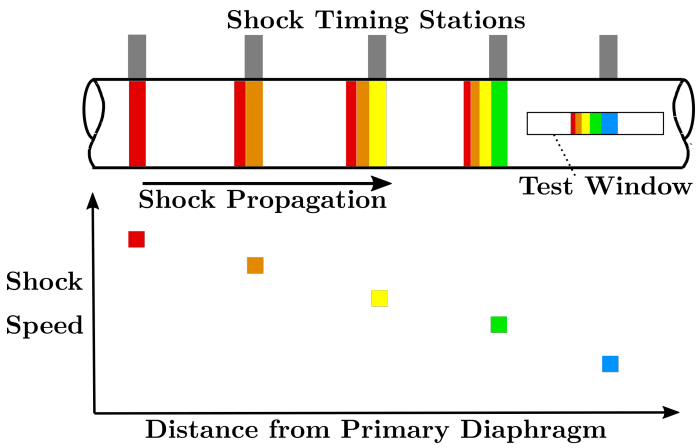

Fig. 3 Individual slices constituting a test slug, coloured by the variable entropy caused by a slowing shock as measured by shock timing stations.

space continuously filled by gas processed by the shock further downstream. As a result, the test slug may be viewed as the sum of a number of infinitesimal slices of gas originating along the length of the shock tube which each undergo compression and acceleration by the shock, and are stacked consecutively to form the entire slug, as seen in Figure 3. The entropy of each slice is set by the shock speed that processed it, and its axial position is determined by the boundary layer mass loss.

The present methodology is built upon tracking the location and properties of discrete slices initially distributed along the tube length. A shock is marched along its trajectory, as recorded by experiment. When the shock reaches the location of each slice, that slice is processed to the post-shock entropy level and an initial total enthalpy. Slice speed is then determined at each point in the remaining shock trajectory by performing a mass balance against the boundary layer. Having determined the slice distance from the shock and its speed, the variation in total enthalpy is computed at each point in the trajectory due both to its variation in speed and also from work performed by isentropic waves. This process is repeated for all the discrete slices, and the final locations and properties of each slice then comprise the extents and properties of the test slug. The entire process is conceptually summarized in the flow diagram of Figure 4. In practice, switching the inner and outer loops is more computationally efficient.

In the following mathematical descriptions, properties referring to the original post-shock state of a slice will be denoted using the superscript t^0, and do not change with time. The original post-shock state is important, since the entropy is held constant from this point, and the total enthalpy at later steps is referenced as changes to this original state. At some later time, the slice is farther from the shock and at the same entropy level, but with a variable total enthalpy as waves from the accelerating shock affect it. The properties of a slice are influenced by the properties behind the shock, and so properties at the slice shall be referenced with subscript E, and post-shock properties shall be denoted by subscript $_{sh}$. However, waves require a finite time to travel between slice and shock. A time level t^+ refers to conditions at the point in the future when an upstream wave co-located with the slice at the current time level t will reach the shock

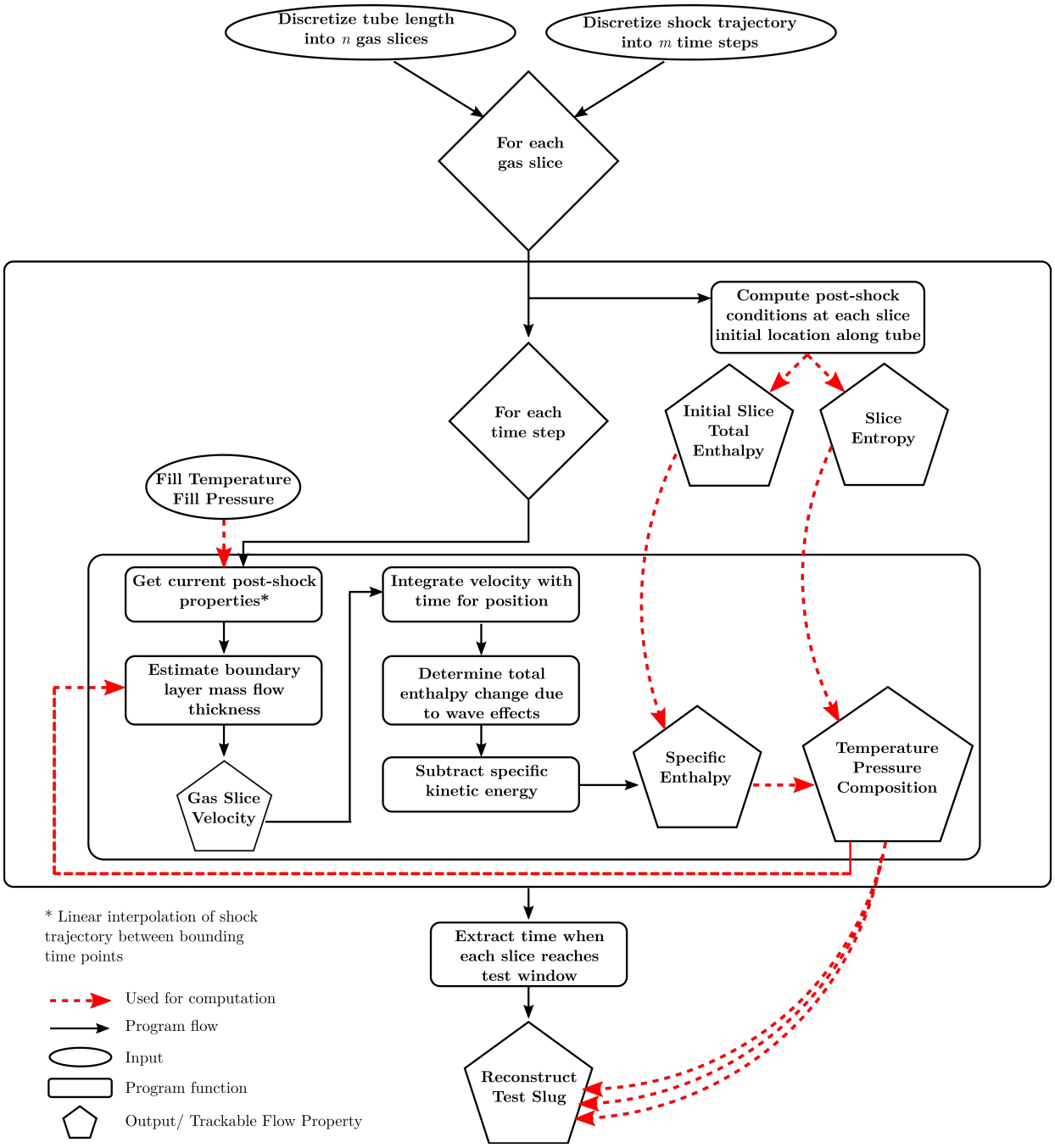

Fig. 4 Flow diagram for the LASTA program.

to influence its trajectory. Time level t^- refers to conditions at the point in the past when the relaxation wave co-located with the slice at time level t was emitted by the shock. Each of these points in time, along with the waves which define them, are shown in Figure 5a, as well as the property locations referenced in each subscript in 5b.

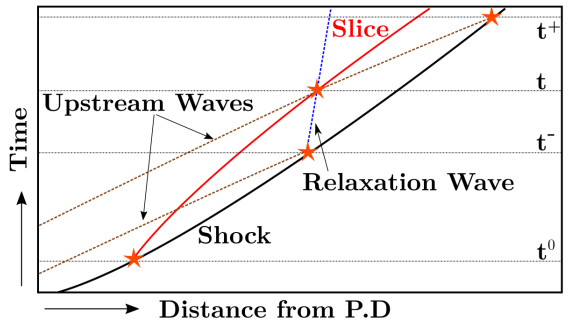

(a) Time levels. Stars denote wave intersections which define each time level.

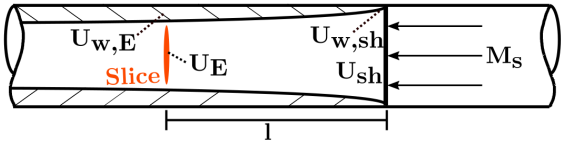

(b) Gas property locations, where U is any flow variable, in the shock frame of reference.

Fig. 5 Schematics annotating the time levels (superscripts) and spatial locations (subscripts) associated with each slice.

The following formulation assumes a laminar boundary layer. However, under many circumstances the boundary layer within the test slug will transition to turbulence. The boundary layer in the present methodology may be computed using the laminar relations described herein until the transition point, after which location the turbulent relations may be used instead as described in Appendix A.

A. Determination of Slice Speed and Location

After each slice is processed by the shock, it is accelerated impulsively to a post-shock velocity, as well as entropy and enthalpy, which may be obtained for the known shock Mach number. The motion of the gas produces a boundary layer along the wall, consuming mass from the inviscid core flow. This in turn causes the core flow to accelerate in the laboratory frame, or decelerate towards stagnation in the shock-stationary frame [1]. Thus, the acceleration of the slice due to mass loss from the core may be found by using a mass balance. Knowing the slice velocity at each point in the trajectory, the slice location may also be integrated. The first step of the formulation is to determine the slice velocity and location. This process is now explained, as well as the means to find the resulting stream tube area, which influences the waves which affect the slice enthalpy.

At the slice location, the total mass flow must be the sum of the mass flow in the boundary layer $\dot{m}_{BL}$ and the mass flow in the inviscid core flow $\dot{m}_{core}$, which together must equal the mass flow processed by the shock, $\dot{m}_{sh}$:

$$\dot{m}_{sh} = \dot{m}_{BL} + \dot{m}_{core} \tag{1}$$

The boundary layer and core mass flows are given as:

$$\dot{m}_{core} = \rho_E u_E \pi (r_{tunnel} - \delta_m)^2 \tag{2}$$

$$\dot{m}_{BL} = \rho_{w,sh} u_w \pi \left\{ r_{tunnel}^2 - (r_{tunnel} - \delta_m)^2 \right\} \tag{3}$$

δ_m is the mass flow thickness as defined by Hooker [23] and improved upon by Mirels [1]. $u_w = u_s$ is the wall speed, which equals the speed of the reference frame (shock speed), and $\rho_w = P_E/(RT_w)$ is the density along the wall, which assumes a cold wall of temperature equal to the pre-shock gas temperature. Plugging in Equations 2 and 3 into 1, the slice velocity in the shock frame of reference u_E may be obtained as:

$$u_E = \frac{\dot{m}_{sh} - \dot{m}_{BL}}{\rho_E \pi (r_{tunnel} - \delta_m)^2} \tag{4}$$

From Hooker [23], the mass flow thickness δ_m for a laminar boundary layer may be calculated by Equation 5 using conditions at the wall and packet distance l from the shock, where $u_{abs} = u_{shock} - u_E$:

$$\delta_m = \beta \left(\frac{\mu_w l}{\rho_{w,E} u_{abs}} \right)^{\frac{1}{2}} \tag{5}$$

Mirels' extensive analysis provided estimates of shape factor β behind a moving shockwave [1], with the result seen in Equation 6.

$$\beta = C_M^{\alpha} 1.59 \left(1 + \frac{1.796 + 0.802W}{WZ - 1} \right) \tag{6}$$

where

$$C_M = \frac{\rho_{sh} \mu_{sh}}{\rho_{w,sh} \mu_w} \tag{7}$$

Here, $W = u_w/u_{sh}$ comprises a measurement of shock strength, where u_{sh} is the post-shock velocity in the current time steps shock's frame of reference, and $Z = \frac{\gamma+1}{\gamma-1}$. The coefficient C_M^{α} accounts for changes to the boundary layer shape due to variations in the freestream. The value of α used herein is 0.48. Note that in Mirels' analysis [1], C_M is based upon the the ratio of freestream properties to those at the wall at time t^0. In order to couple the unsteady shock speed into the boundary layer shape, the current post-shock freestream values were used to compute C_M, implying an instantaneous reshaping of the entire boundary layer with changes in shock speed.

All parameters have now been defined to find the slice speed in Equation 4 for u_E. By integrating the speed of each slice with time, its location may be obtained as well as its distance from the shock.

B. Determination of Displacement Thickness

Prior to returning to discussion of the slice thermodynamic properties, the correlations of Mirels may be further utilised to find the stream tube area for Equation 19. Mirels [24] gives a laminar boundary layer thickness as:

$$\delta = C_M^{\alpha} \left[\eta_{\delta} - I(\infty)\right] \frac{\rho_{w,sh}}{\rho_{e,sh}} \sqrt{\frac{2l\nu_w}{u_{e,sh}}} \tag{8}$$

Here, ρ_e and u_e signify the core flow values. In keeping with the present formulation of boundary layer shape to accommodate the changing shock speed, the post-shock values $_e$ are taken at the current time t post-shock location. The terms η_{∞} and $I(\infty)$ are approximate parameters obtained by numerical integration of the boundary layer equations as performed by Mirels. Since the present study falls within the shock strength ranges established by Mirels in [24], their accuracy was considered acceptable for the demonstrative purposes of this work. In these relations:

$$\eta_{\delta} = \frac{3.20}{\sqrt{1 + 0.543w}} \tag{9}$$

$$I(\infty) = \frac{1.134}{\sqrt{1 + 1.022w}} \frac{\frac{h_r}{he} - \frac{h_w}{he}}{Pr^{0.47+0.029w}} - \frac{1.569}{1 + 0.993w} \frac{(w-1)^2 \frac{u_e^2}{2h_e}}{Pr^{0.045(w-1)}} \tag{10}$$

Finally, the displacement thickness may be given as:

$$\delta^* = \delta - \delta_m \tag{11}$$

Here, Pr is the Prandtl number, and h_r signifies the recovery enthalpy. Equation 11 shall be referenced later in Equation 20 in order to obtain stream tube areas. The coefficients in the Mirels boundary layer equations are obtained from interpolation fits for exact integrations of the compressible boundary layer equations as obtained by Mirels in [25]. These coefficients do not change with different gas species, but do have a weak dependence on Prandtl number which Mirels reports should be negligible for most gases encoutered in shock tubes [1].

C. Variation in Total Enthalpy

At each time in the trajectory, the present conditions of each processed slice are updated by performing an energy balance on it in a shock-stationary frame of reference. Since the slice remains isentropic, all thermodynamic changes

originate in variations in total enthalpy and exchange between kinetic and internal energy:

$$\boxed{H_E^t = H_E^{t^0} + \Delta H = H_E^{t^0} + \Delta h_E^t + \int_{us_1}^{us_2} u_E \partial u_s} \tag{12}$$

Δ is used herein to denote a finite change between discrete states in the slice of gas. The total enthalpy of a given slice is not constant as it travels because of the accelerating frame of reference and pressure waves emerging from a variety of sources, which are accounted for by $\int_{us_1}^{us_2} u_E \partial u_s$ and Δh_E^t, respectively. Both terms are thus computed as the change from time t^0 to time t, as opposed to between consecutive times t. In the inviscid and chemically inert core flow, the only source or sink of total enthalpy must arise from pressure waves, and act directly upon the static enthalpy of the slice. This indicates that the decelerating shock sends waves which reduce the static enthalpy of the gas behind it, while the accelerating shock is associated with waves which elevate the static enthalpy behind it. Expressing the static enthalpy as a function of pressure, then, the change in static enthalpy from t^0 to time t may be written as:

$$\Delta h_E = \frac{\partial h_E}{\partial p_E} \Delta p_E \tag{13}$$

$\frac{\partial h_E}{\partial p_E}$ may be estimated in the case of a chemically reacting gas by solution of a classic entropy/pressure equilibrium problem from, for example, repeated calls to the NASA CEA code [26, 27] in order to produce a local derivative. The computation of the change in pressure at the slice, Δp_E is discussed next.

D. Influences Upon the Slice Pressure p_E

The slice pressure p_E is subject to waves emitted by a number of influences, enumerated in order of diminishing magnitude:

1) Relaxation waves from changing post-shock conditions
2) Waves travelling from upstream which also cause shock acceleration
3) Waves from mass flow absorption by the boundary layer
4) Waves from mixing and reflections at the contact discontinuity

The local pressure was also shown by Mirels [9] to rise as the core flow ‘stagnates’ in the shock frame of reference, accelerated in the stationary frame of reference by mass loss to the boundary layer and exchanging kinetic energy for internal energy, which effect is accounted for later. Since the shock Mach number versus time is provided as an input, the sum of waves which influence shock acceleration such as items 2) – 4) may be treated together as a single wave which will impact the shock and cause it to accelerate at some future time. This approximation is enabled by the domination of waves travelling from upstream in shock speed determination. For conciseness, the sum of the waves which combine to affect shock speed are hereafter referred to as ‘upstream’ waves.

Considering the above, the pressure of an isentropic slice of gas is subject to the influence of one family of waves which travel upstream, and another family of waves travelling downstream, as seen in Figure 6. In the shock frame of reference, all flow in the test slug is subsonic, and so waves are free to propagate both to the shock from any given slice, and also back from the shock to that slice. As a result, the effect of a series of waves upon an isentropic slice with uniform radial properties may be treated by the principle of superposition. In other words, the contribution of each wave upon the pressure may be added to each other for a sum total influence of the waves upon the particle at any instant in time.

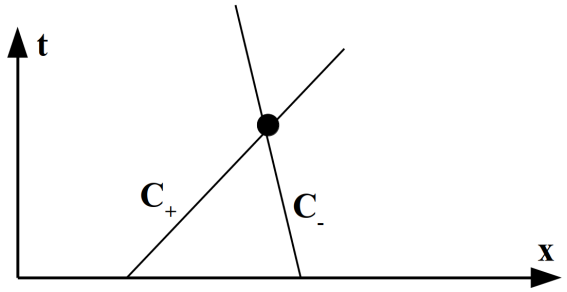

Fig. 6 Propagation of two families of pressure waves across an infinitesimal point in a subsonic flow.

In the test gas behind a moving shock, the Mach number is subsonic in the shock frame of reference throughout the flowfield, and so all slices encounter up- and down-stream oriented families of waves in a non-simple region. Put mathematically, this means that the pressure at a given point in a one-dimensional flow is subject to waves which travel with the left- and right-going characteristics C_- and C_+:

$$\Delta p = \Delta p_{C_+} + \Delta p_{C_-} \tag{14}$$

The left-going waves are the relaxation waves emitted by the shock itself, which travel on the characteristic C_-. The right-going upstream waves travel towards the shock on the characteristic C_+. The change in slice pressure due to relaxation and upstream waves may thus be given by:

$$\Delta P_E^t = \underbrace{\frac{\partial p_E^t}{\partial p_{sh}^t}\Delta p_{sh}}_{\text{Relaxation}} + \underbrace{\frac{\partial p_E^t}{\partial p_{sh}^t}\frac{\partial p_{sh}^{t^+}}{\partial M_s^{t^+}}\Delta M_s}_{\text{Upstream}} \tag{15}$$

In Equation 15, the first term is the influence of relaxation waves as produced by the changing shock Mach number M_s, and the second term is the strength of upstream wave which will reach the shock at some future time, but which is currently passing the location of the slice. Each of the derivatives in Equation 15 are now examined in the following sections,.

1. Amplification and Attenuation of Pressure Waves Due to Travel Through the Test Slug

It is helpful to visualize the core flow as a subsonic nozzle, wherein the walls of the nozzle are formed by the boundary layer and its entrance is at the shock. The relaxation and upstream waves are subject to variations in magnitude as they traverse the nozzle of varying local densities and sound speeds, as well as a changing cross-sectional area as the boundary layer thickens along the slug. Both the shape of the nozzle, and the variation in properties are easily seen in Figure 2. A pressure wave produced at the post-shock location will be amplified or attenuated both by the gas between the shock and the isentropic slice, and also the nozzle shape as it moves rearward. A wave travelling from the slice towards the shock will likewise be attenuated or amplified in an opposite manner. The term $\frac{\partial p_E^t}{\partial p_{sh}^t}$ accounts for this change, and is derived from the characteristic formulation of the Euler equations next.

The quasi one-dimensional Euler Equations in characteristic form may be written as:

$$\frac{\delta}{\delta t}\begin{bmatrix} w_1 \\ w_2 \\ w_3 \end{bmatrix} + \begin{bmatrix} u & \cdot & \cdot \\ \cdot & (u+c) & \cdot \\ \cdot & \cdot & (u-c) \end{bmatrix} \frac{\delta}{\delta x}\begin{bmatrix} w_1 \\ w_2 \\ w_3 \end{bmatrix} = \begin{bmatrix} 0 \\ -uc \\ uc \end{bmatrix} \frac{1}{S}\frac{\delta S}{\delta x} \tag{16}$$

Here, S is the area of the stream tube, u is the local velocity and c is the local speed of sound. Along a characteristic, the following equation relates the pressure change δp to the characteristics as:

$$\delta w_2 - \delta w_3 = \frac{2}{\rho c}\delta p \tag{17}$$

The use of δ signifies that the change applies equally to gradients in time or in space. Assuming a quasi-steady state, Equation 16 may be plugged into Equation 17 in order to obtain:

$$\delta p = -\frac{\rho c}{2S}\frac{\delta S}{\delta x}\left(\frac{uc}{u+c} + \frac{uc}{u-c}\right) \tag{18}$$

Equation 18 describes the general variation of pressure associated with a variation in Riemann variables along a characteristic as influenced by the changing area of the streamtube. Pressure fluctuations at one end of the streamtube will be communicated to the other end of the tube under the same variation. As a result of this similarity, a given pressure wave of amplitude Δp_{sh} which originates with some density ρ_{sh}, speed of sound c_{sh} and stream tube area S_{sh} and travels into a gas with density ρ_E, speed of sound c_E and stream tube area S_E will emerge from its travel at strength Δp_E. Assuming a linear area change $\frac{\delta S}{\delta x}$ =constant, the change in pressure at the slice from a wave originating at the shock then becomes:

$$\frac{\partial p_E}{\partial p_{sh}} = \frac{\delta p_E}{\delta p_{sh}} = \frac{S_{sh}}{S_E}\frac{a_E}{a_{sh}} \quad \text{where} \quad a_* = \rho_* c_*\left(\frac{u_* c_*}{u_* + c_*} + \frac{u_* c_*}{u_* - c_*}\right) \tag{19}$$

S_{sh} is the full tube area, and the area of the stream tube, S_E, is the area of the tube minus the area of the boundary layer displacement thickness:

$$S_E = \pi(r_{tunnel} - \delta^*)^2 \tag{20}$$

The method for obtaining displacement thickness is detailed later. With the amplification or attenuation of waves travelling up or downstream accounted for, the influence of the two families of waves are now examined.

2. Relaxation Waves - The Influence of the C_- Family

Returning to the first term of Equation 15, the C_- family of waves are the waves travelling upstream from the shock towards the slice, changing in magnitude as the streamtube narrows. Since Equation 15 relates the change in enthalpy of the slice from its original enthalpy at time t^0, Δp_{sh} becomes the change in pressure from the time when the slice was first processed by the shock:

$$\Delta psh = p_{sh}^{t^0} - p_{sh}^{t^-} \tag{21}$$

At any time level t, the slice is some finite distance from the shock, but its pressure contains a relaxation wave emitted by the shock at some earlier time t^-. In the frame of reference of the shock, this travelled from the shock towards the slice at speed $c + u$, where the local c and u change as the wave traverses the slug. However, assuming a quasi-steady state in which these conditions change only slowly across the time $t - t^-$, the time which the wave will take to reach the slice may be approximated by using the average values of $\bar{c}$ and $\bar{u}$ throughout the test slug, where u is taken in the shock-stationary frame of reference. Thus, the time in the past at which the shock produced the relaxation wave which currently influences the slice is obtained as:

$$t^- = t - \Delta t_{wave} = t - \frac{l}{\bar{c} + \bar{u}} \tag{22}$$

Here, l is the distance from the slice to the shock. Since the shock trajectory is known, at a given time of computation along the trajectory, the shock speed at the past time t^- is known, and so the value of the post-shock pressure at that time may simply be looked up. The resulting change in pressure Δp_{sh} is then modified by the amplification factor of Equation 19, leading to the form of Term 1 of Equation 15.

3. Upstream Waves - The Influence of the C_+ Family

Shifting focus to the second term of Equation 15, the strength of the wave $\Delta p_{sh}^{t^+}$ required to produce a change of shock Mach number $\Delta M_s^{t^+}$ at time t^+ from the current Mach at time t, $\frac{\partial p_{sh}^{t^+}}{\partial M_s^{t^+}} \Delta M_s$ is now examined. Although the change in shock speed between any two points in time is known, the actual size of the wave required to bring about that change

has not yet been determined. This value may be obtained by evaluation of the conditions required on either side of a Reimann discontinuity to produce a shock wave of a given speed, as seen in Figure 7.

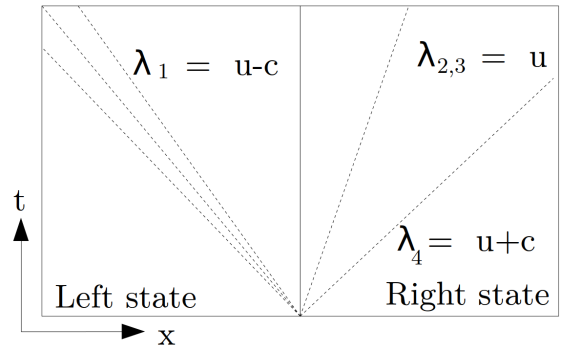

Fig. 7 Wave Speeds Across a Discontinuity

Across a Riemann discontinuity, the speed of the right-going wave λ_4 is given by Roe [28] as:

$$V_s = \lambda_4 = \tilde{u} + \tilde{c} \tag{23}$$

The Roe-averaged variables in one dimension, denoted with a superscript, are computed as:

$$\tilde{u} = \frac{u_L\sqrt{\rho_L} + u_R\sqrt{\rho_R}}{\sqrt{\rho_L} + \sqrt{\rho_R}} \tag{24}$$

$$\tilde{c} = \sqrt{(\gamma - 1)(\tilde{H} - \frac{1}{2}\tilde{u}^2)} \tag{25}$$

$$\tilde{H} = \frac{H_L\sqrt{\rho_L} + H_R\sqrt{\rho_R}}{\sqrt{\rho_L} + \sqrt{\rho_R}} \tag{26}$$

The change in shock speed with respect to a change in the left-state pressure may be obtained by taking the derivative of Equation 23 with respect to pressure.

$$\frac{\partial M_s^{t^+}}{\partial p_{sh}^{t^+}} = c_1^{-1}\left(\frac{\partial \tilde{u}}{\partial p_{sh}} + \frac{\partial \tilde{c}}{\partial p_{sh}}\right) \tag{27}$$

First examining the change in Roe velocity:

$$\frac{\partial \tilde{u}}{\partial p_L} = \frac{\partial \tilde{u}}{\partial \rho_L}\frac{\partial \rho_L}{\partial p_L} \tag{28}$$

$$\frac{\partial \tilde{u}}{\partial \rho} = \frac{\sqrt{\rho_R}(u_L - u_R)}{2(\sqrt{\rho_L} + \sqrt{\rho_R})^2\sqrt{\rho_L}} \tag{29}$$

In the case of a chemically reacting flow, a local derivative estimate of $\frac{\partial \rho_L}{\partial p_L}$ may again be found by multiple solutions

of a constant entropy-pressure equilibrium problem.

Turning now to the Roe speed of sound:

$$\frac{\partial \tilde{c}}{\partial p_L} = \frac{\partial \tilde{c}}{\partial \tilde{H}} \frac{\partial \tilde{H}}{\partial p_L} + \frac{\partial \tilde{c}}{\partial \tilde{u}} \frac{\partial \tilde{u}}{\partial p_L} \tag{30}$$

$$\frac{\partial \tilde{c}}{\partial \tilde{H}} = \frac{\sqrt{\gamma - 1}}{2} \left(\tilde{H} - \frac{\tilde{u}^2}{2} \right)^{-\frac{1}{2}} \tag{31}$$

$$\frac{\partial \tilde{H}}{\partial p_L} = \frac{\partial \tilde{H}}{\partial H_L} \frac{\partial H_L}{\partial p_L} + \frac{\partial \tilde{H}}{\partial \rho_L} \frac{\partial \rho_L}{\partial p_L} \tag{32}$$

In the case of chemically reacting flows, the derivatives of H_L and ρ_L with p_L may again be approximated by use of a local derivative obtained from an equilibrium solver.

$$\frac{\partial \tilde{H}}{\partial H_L} = \frac{\sqrt{\rho_L}}{\sqrt{\rho_L} + \sqrt{\rho_R}} \tag{33}$$

$$\frac{\partial \tilde{H}}{\partial \rho_L} = \frac{\sqrt{\rho_R}(H_L - H_R)}{2(\sqrt{\rho_L} + \sqrt{\rho_R})^2 \sqrt{\rho_L}} \tag{34}$$

$$\frac{\partial \tilde{c}}{\partial \tilde{u}} = -\frac{(\gamma - 1)\tilde{u}}{2\sqrt{(\gamma - 1)(\tilde{H} - \frac{1}{2}\tilde{u}^2)}} \tag{35}$$

Plugging Equations 28-34 into Equation 27 with properties of the left state given as U^t_{sh} and properties of the right state as U_1, and inverting, the change in pressure required to bring about a given change in shock speed is found from:

$$\frac{\partial p^{t^+}_{sh}}{\partial M^{t^+}_s} = \frac{1}{\frac{\partial M^{t^+}_s}{\partial p^{t^+}_{sh}}} = c_1 \left(\frac{\partial \tilde{u}}{\partial p_{sh}} + \frac{\partial \tilde{c}}{\partial p_{sh}} \right)^{-1} \tag{36}$$

The change in Mach number ΔM_s is computed as the change in shock Mach number from the time t to t^+. As with the relaxation waves, the finite distance between shock and contact discontinuity causes a finite time of travel for the wave of interest. The wave presently influencing the slice at t will influence the shock at a future time t^+, and this time may be found from Equation 37.

$$t^+ = t + \Delta t_{wave} = t + \frac{l}{\bar{c} - \bar{u}} \tag{37}$$

Note that Equation 37 differs from Equation 22 by the sign of contribution of the local velocity, causing the upstream wave to traverse the test slug more slowly than the relaxation waves. Having found the time in the future t^+ at which the

upstream wave will reach the shock, $\Delta M_s^{t^+}$ may then be determined. Near the end of the trajectory, the shock speed that might be achieved at time t^+, absent disturbances at the end of the tube such as a dump tank, may not be known.

In circumstances where the shock trajectory beyond the test section are unknown, as is often the case in experimental setups, the shock trajectory may simply be extrapolated under an implicit assumption that no strong upstream waves such as a reflected expansion will influence the shock shortly past the known trajectory data. The presence of any strong waves in the test slug near the end of the tube would substantially influence the properties of the test slug, and so such a situation is typically avoided in experimental setups e.g. by piston tailoring in a free-piston shock tube facility. In the characterisation of flow properties in a completed experiment, readings from a pressure transducer located just prior to the test section may be used to minimize this limitation by modifying the extrapolated trajectory to match the measured static pressure. The potential errors introduced by this practice are discussed in-depth in a later paper [21].

Returning to Equation 15, the original strength of the upstream waves thus determined is now seen to be modified by the inverse of the characteristic modification term $\frac{\partial p_E}{\partial p_{sh}}$, since the upstream waves must travel down the nozzle in the opposite direction from the relaxation waves travelling up it:

$$\frac{\partial p_E}{\partial p_{sh}^{t^+}} = \frac{1}{\partial p_E / \partial p_{sh}} \tag{38}$$

Finally, the change in total enthalpy due to the moving frame of reference is given as:

$$\int_{us_1}^{us_2} u_E \partial u_s = u_E \left(u_s^t - u_s^{t^0} \right) \tag{39}$$

All terms in Equation 13 have been defined and the change in enthalpy of an isentropic slice resulting from variations in shock speed may now be computed.

With all parameters for Equation 12 now determined, the total enthalpy of the slice at the present time step t can be computed by use of Equation 12. Obtaining $h_E^t = H_E^t - \frac{1}{2}u_E^2$, the static enthalpy and entropy for the slice is known, and so the other thermodynamic properties may be computed. In the case of an equilibrium chemically reacting flow, the properties may be obtained from solving a constant enthalpy-entropy equilibrium problem.

The above analysis reflects the development of only a single slice of gas. However, repeating this process for a number of slices processed at different points along the tube, the properties and locations of each slice are known at the end of the tube. For example, a plot of temperature versus location for all the slices should be an accurate representation of the temperature throughout the test slug as might be measured by a stationary sensor in the test section. Simultaneously, the pressure and other properties of the entire test slug, along with the development history of each portion represented by a slice is also known.

E. Limiting the Variation of Pressure

In the above development, the conservation of mass and energy are coupled and solved for each individual slice by combining several simplified models for various aspects of the flow. However, the conservation of momentum is never ensured. Each slice is tracked individually and unable to communicate its momentum in exchange for pressure with the other slices in the test slug, despite its being a subsonic flow in the moving frame of reference. As a result, the absence of the momentum equation leads to an inability to capture the effect of momentum exchanged for pressure behind the shock as its post-shock velocity shifts. At a constant shock speed in an inviscid flow, the post-shock momentum will be constant. However, if the shock suddenly decelerates, it will produce a lower post-shock momentum, and the faster-moving, heavier gas from earlier in the trajectory will collide with the new slower, less compressed gas, producing a compression wave. In addition to its travel towards the shock as an extra source of upstream wave, this wave should travel to the rear of the test slug. As it does so, the wave should influence the pressures throughout. Furthermore, the rearmost slices will have been exposed to the most such waves throughout the trajectory and traded the most momentum, and so this effect is most pronounced at the rear of the test slug. It is important also to note that the effect of momentum exchange is isentropic in nature. Without inclusion of this effect, the detailed methodology under conditions of strong shock deceleration will show a non-physical drop in pressure towards the rear of the test slug.

Rather than obtaining an approximation or a more expensive full solution of the complex interchange of pressure and momentum throughout the test slug, the effects of the lack of momentum conservation may be accounted for indirectly. It may be observed in Satchell *et al.* [10] that the static pressure traces behind both accelerating and decelerating shocks increase monotonically until the contact discontinuity, even for strongly decelerating shocks. Thus, by imposing upon the slices in the present methodology a constraint wherein the pressure must not decrease moving upstream from the shock, the influence of momentum exchange may be accommodated by enforcing its ultimate effect. At the end of each time step, if the pressure of a slice is found to drop below that of a slice immediately downstream of it, the upstream slice pressure is isentropically elevated to match that of the downstream slice, and its other thermodynamic variables accordingly recomputed. The result is a static pressure through the test slug which is, under all conditions, monotonically increasing or constant while maintaining the condition of isentropy for all slices.

IV. Implementation of Quasi One Dimensional Model

Development of the methodology described above, entitled for reference herein as the LAagrange Shock Tube Analysis (LASTA) methodology, centered around the tracking of an individual slice processed by the shock at some arbitrary time along the shock trajectory. However, by repeating the methodology across numerous individual slices distributed along the tube, the entire test slug may be reconstructed. For each slice, the variation of static enthalpy at each timestep was computed using the master Equations 12, 13 and 15, where the terms for each are computed as detailed above. The LASTA methodology was implemented in the Python programming language. The tube inputs

to LASTA are the fill gas pressure, temperature and composition, the geometry of the shock tube (tube length and diameter), history extraction locations and the initial location of the Lagrangian slices and time steps.

V. Validation

LASTA was validated against a series of numerical simulations by Satchell *et al.* [10] as all data is known at fine time and spatial resolution. As these are perfect gas simulations, they allow direct validation of the wave processes without the complications of thermochemistry. Further application of LASTA for true experimental data, different geometries and equilibrium thermochemistry models is provided in the associated paper [21].

A. Test case Setup

Three shock tube simulations of varying shock speed profiles are used as test cases produced using the FROSST code [4], which is an axisymmetric Navier-Stokes DNS-like solver developed specifically for shock tube simulations. These results are detailed in Satchell *et al.* [10]. Depending on the type of driver gas compression and diaphrgam opening profile, periods of acceleration, deceleration and constant speed are common in shock tube experiments. Accordingly, a monotonically accelerating, monotonically decelerating, and a nearly constant-speed shock trajectory were selected so that the behavior of the LASTA methodology could be studied in the context of each type of case. The selected shock trajectories may be seen in Figure 8. All three cases result in a shock speed of 2100 m/s at the end of the tube. Argon was used for the test gas, enabling study of wave effects in the absence of thermochemical effects. Fill pressure was 66.7 Pa and fill temperature was 300 K. The tube geometry was 100 mm in diameter and a length of 8 m.

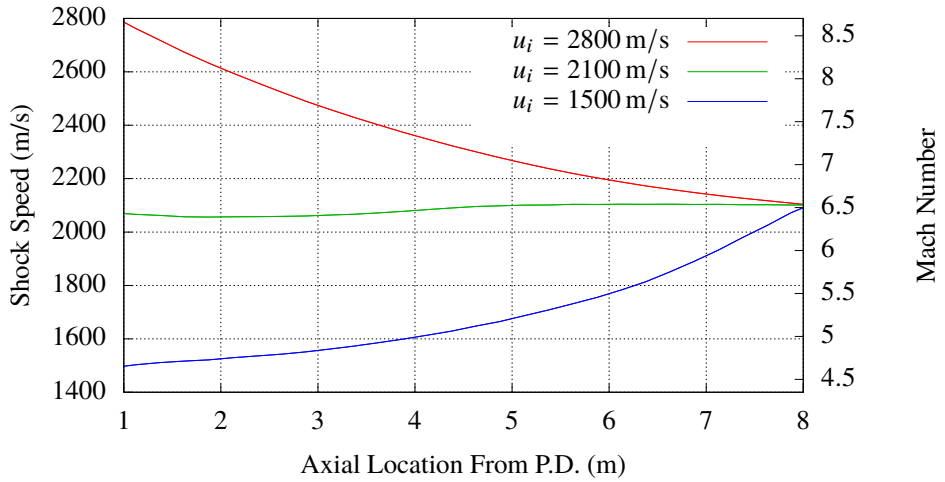

Fig. 8 Three shock trajectories arriving at the same shock Mach number at the end of the tube.

LASTA was run using 75 slices distributed evenly along the tube, and each was tracked with a time step of 3 μs for all shock trajectories. The last time step was computed when all slices on a given trajectory had reached an axial distance

of 8 m from the start of the tube, and the slice conditions and timestamp when each slice crossed that location were recorded. This creates a property trace directly comparable against the centerline data computations of FROSST [10]. Each trajectory required an average of 3.76 s in order to run all 2000 time steps on a single Intel®Xeon(R) W-2155 CPU @ 3.30 GHz core with 31 GiB memory. A perfect gas behavior and a laminar boundary layer were assumed in the present study.

B. Overall Results

The resulting comparisons of pressure and temperature against the results of Satchell *et al.* [10] are shown in Figure 9. The end of the test slug in FROSST is signaled by the arrival of cold driver gas, visible in Figure Test 9 by the sudden drop in temperature and marked by the vertical dotted line for each case. LASTA computes only test gas, and so the end of the test slug in the LASTA plots is simply the final slice. The LASTA method is seen to reproduce all test slug temperatures to within 1% for the entire length of the test slugs in the multidimensional Navier-Stokes simulations. Pressure is also within 1% for pressures throughout all test slugs, except the very rear of the accelerating case. Here, a jet of driver gas is seen to arrive at 220 μs, at which point the LASTA pressure prediction agrees to within 3.5%. The source of this small discrepancy is believed to arise in the reflection from the contact discontinuity of compression waves produced by the accelerating shock within the FROSST simulation. Although the effect of such reflected waves upon shock trajectory would be captured in part by the upstream waves contribution in LASTA, their lingering and direct influence upon the slices themselves is not captured by the methodology. Since strong and monotonic acceleration is not common in actual shock tube experiments, this circumstance is considered to be an extreme.

Time is overpredicted by the LASTA methodology for the accelerating and decelerating cases. The overprediction of test time has two sources. The first is due to the inability of the one-dimensional code to predict a jet which emerges along the wall in the highly accelerating case to contaminate the rear 35% of multidimensional test slug. This jet is due to the elevating pressure in the test slug, which causes the contact discontinuity to lose containment of the driver gas through the boundary layer. The jet is observable in the two-dimensional Navier Stokes simulation results by the gradual decline in temperature in that case as opposed to the comparatively sharp declines seen in the other cases. Examination of the temperature profiles reveals that the LASTA method agrees strongly with the rearmost location of each contact discontinuity, which is visible as a steadying of the cooling temperature. This observation provides further evidence that the method accurately predicts the primary flow behaviours, but is hampered by the contamination. In agreement with the analysis of Hooker [23], the presence of strong mixing at the contact discontinuity adds considerable uncertainties to any evaluation of the rear portions of the test slug in either the multidimensional simulation or even experiments, and so the overprediction at rear of the test slug is considered acceptable. The second source of disagreement in test time is the consumption of test gas by the boundary layer. Although LASTA is able to turn off slices whose boundary layer mass flow exceeds the core mass flow, additional test gas also slides down the contact discontinuity and out of the test slug

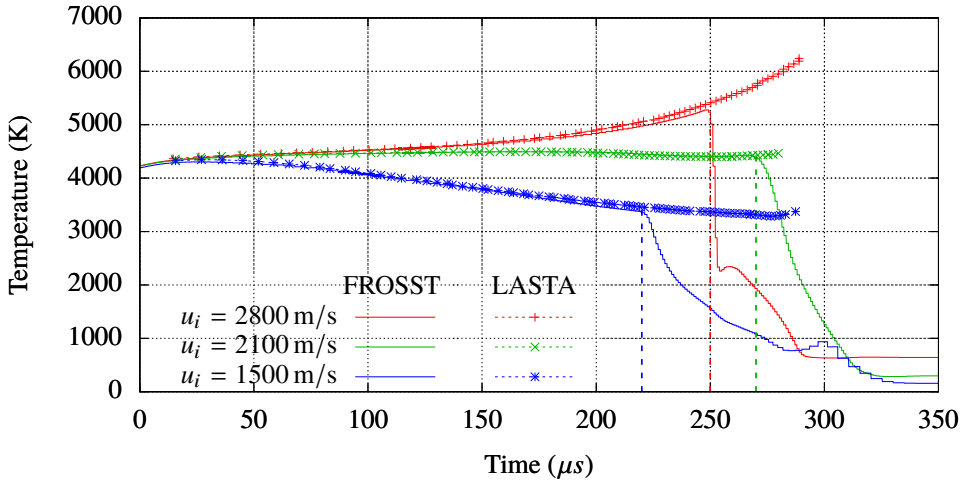

(a) Temperature Profiles for All Cases

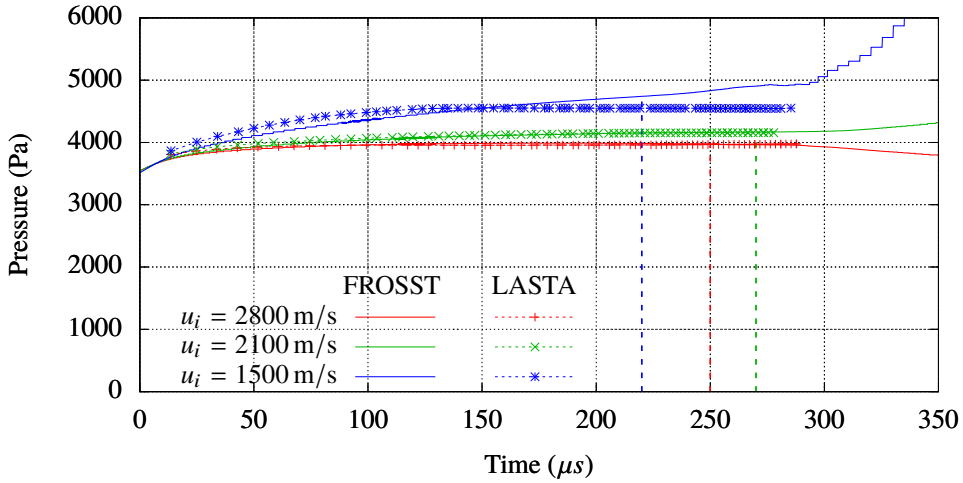

(b) Pressure Profiles for All Cases

Fig. 9 Test slug reconstructions for five shock trajectories, FROSST vs the LASTA method.

[10]. As a result, the oldest slice shown in Figure 9 originates near 1 m, whereas the gas at the rear of the test slug in FROSST originated around 3.5 m.

C. Sub Model Interrogation

Although the quasi one-dimensional methodology detailed in this paper has been shown to reproduce the core flow properties to reasonable accuracy, the individual components of the model each have their own assumptions and limitations. It is therefore necessary to investigate the accuracy of each of these models in the context of the unique challenges presented by each shock trajectory. The following discussion is presented for the purposes of illustration and analysis of the limiting assumptions in the methodology, with a focus on the foundational processes of individual packet evolution. In particular, the boundary layer and mass loss model, and also the upstream and relaxation wave models are

examined. Additionally, the use of a practical constraint of the pressure is examined.

A gas slice originating at $x = 4$ m from the diaphragm was interrogated for each of the cases. This originating location was selected because the final slice location should sit near the rear of the test slug under the present conditions, but remain well ahead of any jets or vortices which form around the contact discontinuity [10]. The relatively long lifetime of these packets ensures maximal exposure to the relaxation effects described above, making them ideal for assessment of the methodology. The axial location and properties of this slice were then compared against a corresponding massless Lagrangian particle tracked in the FROSST simulations, originating along the centreline at the same axial location. The details of this implementation are given in [10]

1. Modelling of the Boundary Layer and Mass Balance

Firstly, the nearly constant speed shock trajectory at 2100 m/s is examined. The axial velocity of the slice is a direct result of the mass balance from the mass flow thickness as predicted by Mirels. The axial velocity also determines the test slug length by establishing the location of each slice. Thus the accurate capture of velocity and location indicate an accurate representation of boundary layer properties. Coupled to the slice pressure by virtue of the wall density in Equation 5, accuracy of the axial velocity is also both highly sensitive to and broadly determines the accuracy of the total enthalpy balance. The comparison between the gas packets of FROSST and the slices of the LASTA methodology are seen in Figure 10 for the constant-speed shock.

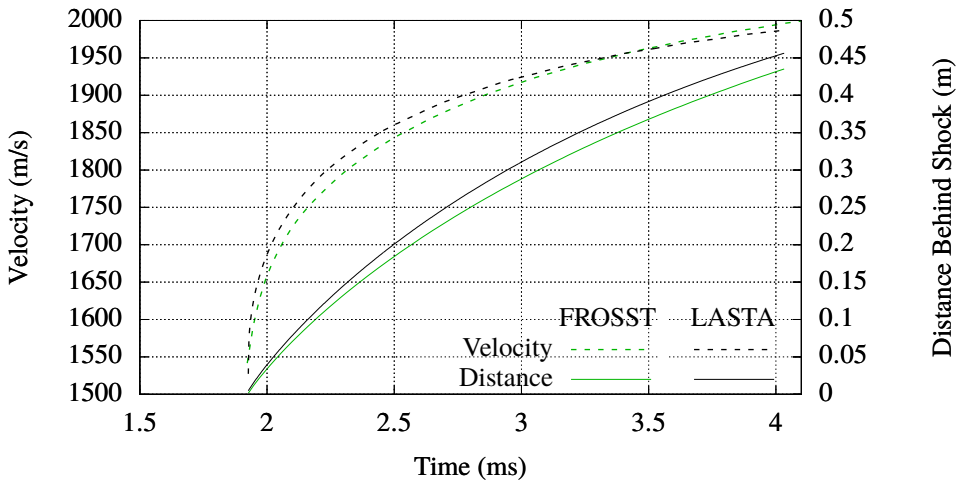

Fig. 10 Variation in velocity and position with time for a slice of gas originating at 4 m as processed by FROSST and LASTA for the constant-velocity shock case.

Slice axial velocity may be seen to match the FROSST gas packet velocity to within 1.1% at all times, integrating to a 1.1% difference in final position by the end of the tube, although this interestingly amounts to a 4% difference in distance behind the shock. Since FROSST has been shown [4] to accurately capture shock tube flows, including the boundary layer, this strong agreement indicates that the mass flow thickness, and resulting mass balance is accurately predicted by

Mirels' estimates. This close matching is also a weaker but significant indication of static pressure agreement, since the boundary layer thickness is sensitive to the wall and core flow densities in Equations 2-4, which are in turn set by pressure in the isentropic slug. By matching the velocity and thereby location of each slice, the level of entropy at the final location of the slice within the test slug is also guaranteed to match. Consequentially, determination of the other properties at that location rests solely upon accurate capture of enthalpy variations due to wave effects.

2. Modelling of Upstream and Relaxation Waves

The accuracy of the speed and integrated position calculations demonstrates the accuracy of the boundary layer and mass balance formulations. The ability to capture the relaxation and upstream waves is now investigated. The total enthalpy balance for these ideal gas cases explicitly determines the temperature at each time step. In the constant shock speed case, the total enthalpy is spatially uniform across the shocked test gas, and so property variations arose only from shifts in velocity. However, in the presence of a variable shock speed, the relaxation waves combine with the upstream waves in Equation 15 to modify the static enthalpy of the slice. Thus, accurate capture of the unsteady temperature and pressure history of the slice reflects accurate modeling of the influence of these waves upon the total enthalpy of the slice.

Figure 11 compares the variation in slice pressure and temperature for each of the cases. In the constant speed case which is absent wave effects, 1.3% agreement is obtained for both pressure and temperature at all points in time, as seen in Figure 11a, with nearly identical matching by the end of the trajectory. The slight waviness in both data sets is due to small variations in shock speed near the end of the trajectory from the shock speed estimates of FROSST. Examining next the decelerating case, temperature in Figure 11b is seen to match to within 0.5% throughout the trajectory. The agreement in pressure for the decelerating case was also within 1%. Examining the accelerating case, Figure 11c shows that temperature is seen to match to within 0.5%, while agreement to 1.3% is seen in pressure throughout its trajectory, diverging from well within 1% only at the very end of the test. This divergence is considered due to the FROSST slice falling under the influence of contaminating driver gas.

This close agreement across all three case types suggests that the wave contributions to static enthalpy are accurately captured, within the restrictions of their limiting approximations. Although the wave calculations account for the time of travel of each wave contribution, the approximation of frozen properties through the test slug throughout the wave's travel would introduce a further degree of time lag error. Finally, both types of waves are subject to a small degree of amplitude error because of the same assumption of frozen test slug properties. As the speed of the shock increases, the length of the test slug shortens and so the time available for such errors to compound is reduced, and so this method is anticipated to remain accurate at higher shock Mach numbers.

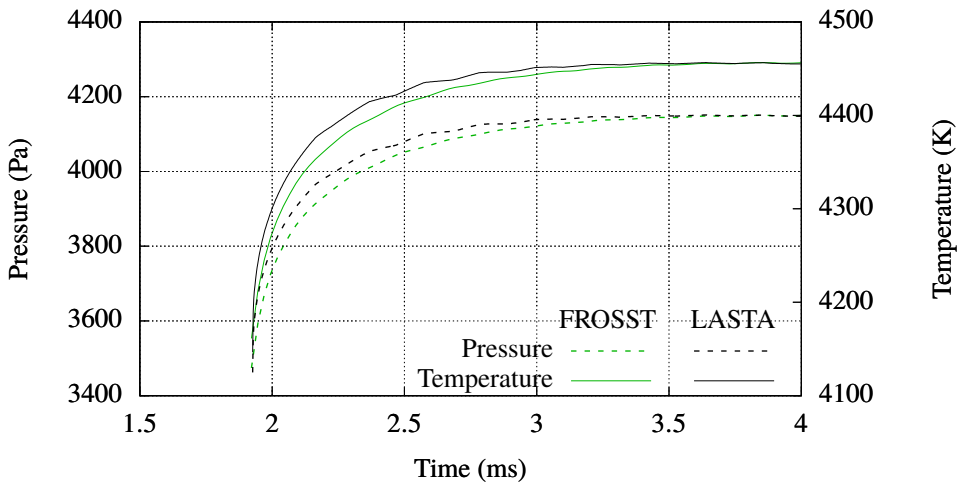

(a) Constant-velocity shock case.

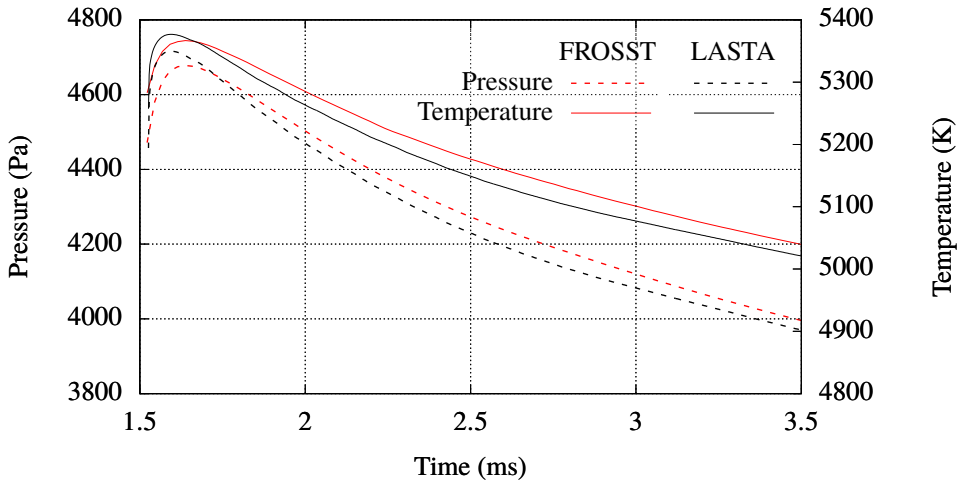

(b) Decelerating shock case.

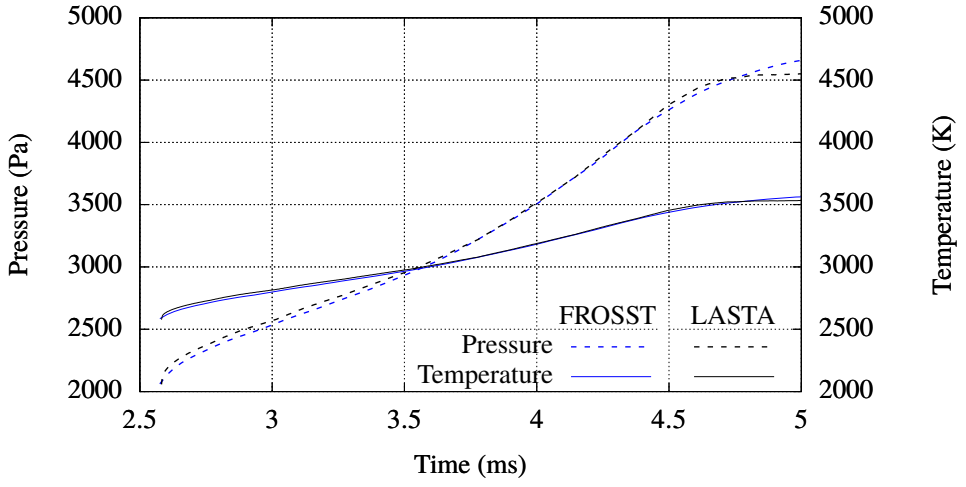

(c) Accelerating shock case.

Fig. 11 Variation in pressure and temperature with time for a slice of gas originating at 4 m as processed by FROSST and LASTA for the each of the three cases.

3. Influence of the Pressure Constraint

The influence of the constraint which prevents the pressure from dropping along the test slug may be evaluated in the context of the decelerating case, for which the effects are most pronounced. Figure 12 shows that the slice pressure is elevated steadily by the influence of downstream slices as compared to the unconstrained case. As the shock slows, the post-shock pressure reduces, allowing the slice to lower in pressure as the expansion waves reach it. However, the presence of the pressure constraint reduces the degree to which the pressure would drop absent an accounting of momentum exchange.

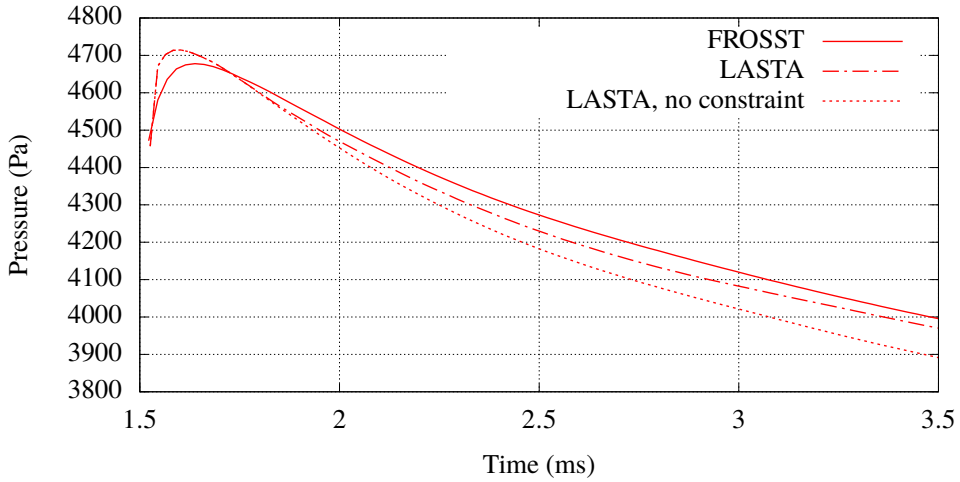

Fig. 12 Comparison of slice pressure history for the LASTA methodology with and without the pressure constraint, plotted against centreline gas packet of FROSST. All packets originated at $x = 4$ m in the decelerating shock case.

VI. Model performance in the presence of strong upstream waves

The cases thus far examined have deliberately limited the potential influence of upstream waves in order to focus on the effects of shock history alone. However, the LASTA method must be validated to show its proper function in the context of more complex upstream waves representative of real experiments. Similar simulations as described previously were performed in FROSST using the same facility geometry as the above discussion, varying driver section length and finite diaphragm opening times to produce different shock profiles. LASTA was then run against these shock profiles and the results compared, as shown in Figure 13. Finally, physical hypersonic shock tubes range in diameter from 50 mm or less through many hundreds of millimeters, causing boundary layer effects to play more or less dominating roles on the dynamics of the test slug. The accuracy of LASTA in the context of a wider tube is shown in Appendix B.

Comparing Cases A and B, and consistent with the findings of [10], it is evident that only a small amount of the gas from the period influenced by the slower initial shock speed remains present in the test slug. However, its presence causes a deviation in temperature for the rear 20% of the test slug. The agreement of these two cases almost identically

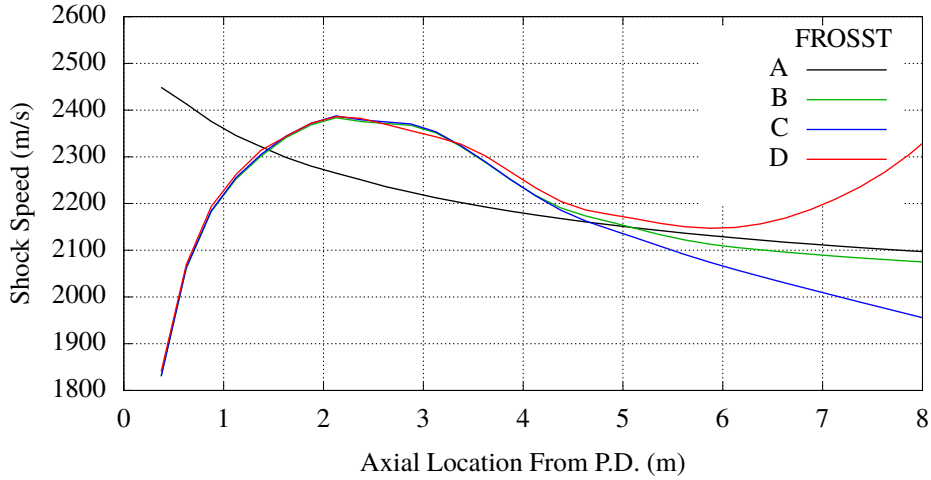

(a) Shock speed profiles for cases involving complex upstream waves.

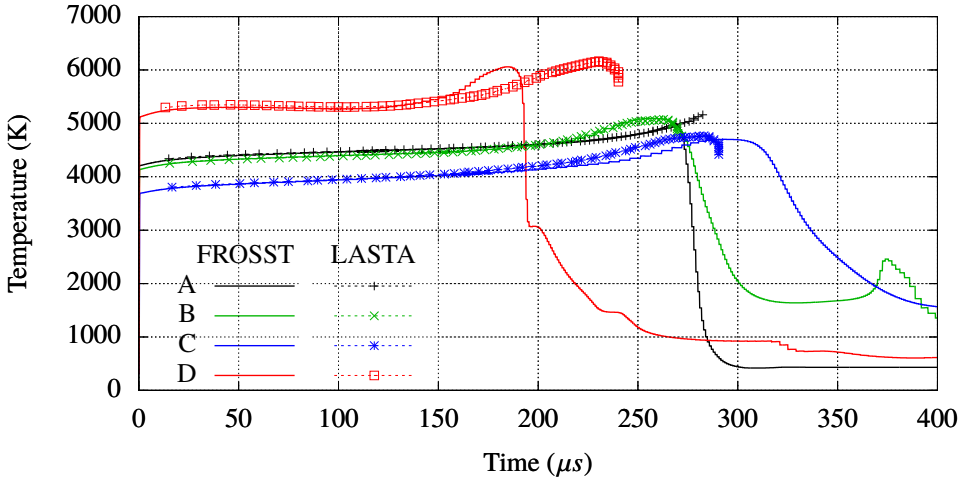

(b) Test gas temperature profiles.

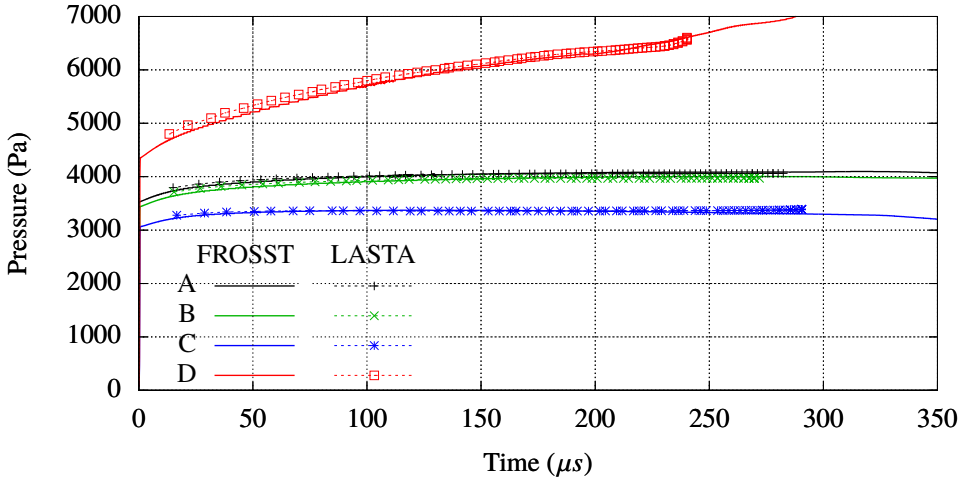

(c) Test gas pressure profiles.

Fig. 13 Shock trajectories and resulting test gas traces in the presence of complex upstream waves.

with FROSST, offset by the small difference in end-tube shock speed, indicates that only the test gas which survives contributes meaningfully to the state of the test gas. Put differently, a LASTA simulation starting after 3 m, which is the originating location of the oldest surviving test gas, would contain all necessary information to match the full numerical simulation. This convenience was tested and confirmed to be true. LASTA agrees to within 1% for both pressure and temperature for these relatively simple cases.

Case C likewise shows excellent agreement between FROSST and LASTA to within 1% for the entire test slug, with a 7% shorter test time predicted by LASTA. The longer test time predicted by FROSST is due to the strong reflected expansion wave pulling on the contact discontinuity, smearing it significantly and extending the test time. This effect may be observed by comparing the FROSST temperature profiles of Cases B and C, where Case C shows a more stretched contact discontinuity. LASTA does not possess a model to capture this, and so cannot match the test time perfectly, but the difference is considered to be acceptable.

Examining Case D, the influence of the acceleration is evident in the highly different trend in pressure and, more subtly, the bulk of the temperature trace which decreases, rather than increasing monotonically compared to the other cases. The overall trends and peak temperature are seen to agree to within 1.7%, and pressure to within 1%. However, the FROSST simulation is seen to predict a significantly shorter test time. Referring to the earlier description of the contaminating jets, the presence of the jet and its resulting vortex is clear in the FROSST results, as seen in Figure 14. The jet has the effect of pushing the test gas forward and also contaminating it, resulting in the shorter test time. As with the high acceleration case of Figure 11, however, the LASTA prediction can be seen to correctly locate the rear of the jet. This agreement gives further confidence in the proper function of the LASTA mass balance computations, although it cannot match the complex multidimensional influence of the jet along the wall. It may also be noted that, although variations in test slug temperature is similar to other cases, a large variation in pressure through the test slug is evident when compared to the other cases. This variation would have a pronounced effect on any thermochemical processes and radiative emissions. As such, the ability to match the pressure under this strong variation is highly important.

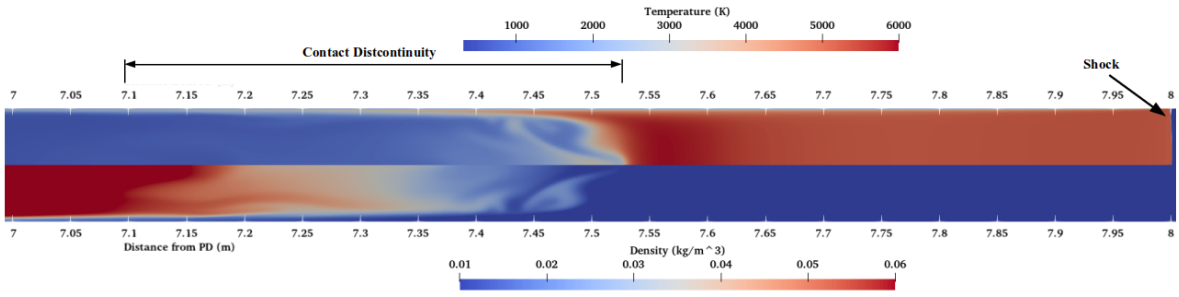

Fig. 14 Extended interface vortex caused by end-tube shock acceleration in Case D. Shock located at 8 m.

A final interesting facet of the above cases is the notable clustering of slices towards the rear of the test slug. This bunching is caused by the non-uniform acceleration of the various slices, with the rearmost slices accelerating the most

due to boundary layer mass consumption. Although strictly qualitative in nature, the agreement in this behaviour with the descriptions of Hooker [23] and Mirels [9] lends confidence that the interaction between boundary layer and core flow is modelled correctly.

VII. Conclusions

An analytical framework to model shock tube experiments has been developed and presented. This accounts for the non-ideal effects from the driver/diaphragm rupturing and boundary layer growth on the resulting shock speed and thus flow properties and position of the shocked test gas at end of the tube. The method assumes the gas is in thermochemical equilibrium. This methodology takes as input the shock speed history along the tube, along with tube fill conditions, thus enabling the modelling of every experimental test individually. This methodology functions by examining the right- and left-going waves which interact with each isentropic slice of shock-processed test gas. These individual slices then combine to form the entire test slug. The functionality of individual portions of the method, particularly the evolution of individual shock-processed gas slices, was validated against Lagrangian gas packets tracked in the axisymmetric Navier-Stokes FROSST solver for the same cases. Individual slices were shown to agree to within 3% on temperature and pressure throughout the slice trajectory. Combining 75 such individual slices, the final temperature and pressure profiles in test slugs for three shock trajectories ending in the same end-tube Mach number were reproduced to within 1% for all cases but one, which agreed to within 1% until the rear of the test slug, which then stayed within 3% agreement. Cases involving complex non-ideal facility waves were also simulated by both FROSST and LASTA, and also showed excellent agreement. Although this paper focused on demonstrating the accurate capture of wave effects in the context of an ideal gas, the methodology thus developed is also accurate with gases in thermochemical equilibrium and using experimental data das inputs. Such applications, as well as additional validation of the LASTA methodology, are given in a later paper [21].

Appendix A: Boundary Layer Equations for a Turbulent Flow

The LASTA methodology as described above assumes a laminar boundary layer. However, the boundary layer will transition to turbulence under many circumstances. In such cases, the mass flow consumed by the boundary layer will increase significantly, while simultaneously increasing core flow restriction. This reduction in inviscid flow area is accompanied by an elevation of the wave amplification factor $\frac{\partial p_E}{\partial p_{sh}}$, as well as a greater degree of clustering of the slices, thereby influencing the enthalpy recovery as well. As a result, both the test time and core flow thermodynamic properties may be anticipated to shift substantially from laminar predictions in the presence of a turbulent boundary layer. The following equations may be used in the LASTA methodology if a turbulent boundary layer is suspected. Either the entire test slug may be assumed turbulent, or some transition model such as the integrated Reynolds number proposed by Weilmunster [29] may be used in order to cause the boundary layer predictions to switch between the

laminar and turbulent equation sets.

Mirels published predictions for the test time of a shock tube with a turbulent boundary layer in the test slug based upon an analysis of boundary layer mass flow consumption [30]. The same basic form of Equation 5 applies as with the laminar case, but the formulation of β changes substantially. It is instead given for turbulent flow as:

$$\beta = \beta_0 \left[\frac{W^2 + 1.25W - 0.8}{W(W - 1.0)} \right]^{0.8} \tag{A1}$$

Here, β_0 is the shape factor which would be predicted for uniform post-shock properties, and is given as:

$$\beta_0 = \frac{p_\infty}{p_0} \frac{W}{W - 1} K_0 \tag{A2}$$

The factor K_0 is essentially a Karman-type shape factor which varies with shock strength and wall temperature:

$$K_0 = 0.0575 \frac{\delta^*/\delta}{1 - W} \frac{1 - W^{0.8}}{\theta/\delta} (W - 1)^{1.8} \left[\frac{\mu_m}{\mu_w} \frac{\rho_w}{\rho_{sh}} \left(\frac{\rho_m}{\rho_{sh}} \right)^3 \right]^{0.2} \tag{A3}$$

The peculiar form of Equation A3 is driven by the need to find the terms $\frac{\delta^*/\delta}{1-W}$ and $\frac{1-W^{0.8}}{\theta/\delta}$ independently by numerical integration:

$$\frac{\delta^*/\delta}{1 - W} = \frac{1}{W - 1} \left\{ 7 \frac{h_{sh}}{h_w} \int_0^1 \frac{\zeta^6 [W - (W - 1)z]}{D} d\zeta - 1 \right\} \tag{A4}$$

$$\frac{\theta/\delta}{1 - W^{0.8}} = 7 \frac{h_{sh}}{h_w} \int_0^1 \frac{\zeta^6 [W - (2W - 1)z + (W - 1)\zeta^2]}{D} d\zeta \tag{A5}$$

and

$$D = 1 + \left(\frac{h_r}{h_w} - 1 \right) \zeta + \left(\frac{h_r}{h_w} - \frac{h_{sh}}{h_w} \right) \zeta^2 \tag{A6}$$

Equations A4-A5 must be integrated numerically using the shock speed at each time step. The recovery enthalpy h_r is taken as the post-shock recovery enthalpy in the absolute frame of reference. h_m is a reference enthalpy akin to the Eckert reference temperature [31], which is designed to adjust the shape factor K_0 to account for the variation of temperature in the boundary layer due to a cold wall beneath a hot flow. It is given as:

$$h_m = 0.5 h_{sh} \left(\frac{h_w}{h_{sh}} + 1 \right) + 0.22 h_{sh} \left(\frac{h_r}{h_{sh}} - 1 \right) \tag{A7}$$

The associated density ρ_m at the reference enthalpy h_m is found by solving a pressure-enthalpy equilibrium problem for a gas in chemical equilibrium.

It must be noted also that the mass flow thickness is treated as the same as the displacement thickness in the

formulation presented by Mirels for turbulent flow, although the two are held distinct in the laminar case. The Eckert coefficients were derived for air, but vary in sufficiently small magnitudes with changes in gas properties that they are typically accepted as accurate for other gases, as well [32]. The coefficients in A1 are based on correlations from the integrated boundary layer equations, and Mirels notes that they are accurate for both air and argon to within 2% for w > 2 [30].

Appendix B: Application of LASTA to a 200 mm Diameter Tube

Tube diameter was doubled to 0.2 m from the cases of Figure 13 in order to show the scalability of Mirels' estimates, as well as the resulting mass balance in LASTA. In the wider tube, the boundary layer comprises a much smaller percentage of the total flow area, and so viscous effects are greatly reduced. Figure B1 shows the much longer test time resulting from the wider tube, as well as the faster shock speed due to fewer viscous losses.

Pressure and temperature both agree to within 1% for the entire test slug, confirming that the mass balance scaled appropriately. With the wider tube, little test gas is lost to the boundary layer, and so the entire shock history is retained, as opposed to only the last 4 m as with the other cases. Since the first metre is dominated by unsteady viscous effects and the initial formation of the shock, some extent of disagreement is anticipated at the rear of the test slug, and so this small disagreement is not considered problematic.

VIII. Acknowledgements

The authors would like to thank the US Air Force for their support of this effort.

References

[1] Mirels, H., "Test Time in Low-Pressure Shock Tubes," *Physics of Fluids*, Vol. 6, No. 9, 1963, pp. 1201–1214. https://doi.org/10.1063/1.1706887.

[2] Morgan, R. G., and Gildfind, D. E., "Shock Tube Simulation of Low Mach Number Blast Waves," *29th International Symposium on Shock Waves 1*, Springer International Publishing, 2015, pp. 83–88. https://doi.org/10.1007/978-3-319-16835-7_11.

[3] White, D. R., "Influence of Diaphragm Opening Time on Shock-Tube Flows," *Journal of Fluid Mechanics*, Vol. 4, No. 6, 1958, p. 585–599. https://doi.org/10.1017/S0022112058000677.

[4] Satchell, M., Collen, P., McGilvray, M., and Mare, L. D., "Numerical Simulation of Shock Tubes Using Shock Tracking in an Overset Formulation," *AIAA Journal*, 2021, pp. 1–11. https://doi.org/10.2514/1.j059829.

[5] Chandel, D., Nompelis, I., and Candler, G., "Computations of High Enthalpy Shock-waves in Electric Arc Shock-Tube (EAST) at NASA Ames," *2018 AIAA Aerospace Sciences Meeting*, American Institute of Aeronautics and Astronautics, 2018. https://doi.org/10.2514/6.2018-1722.

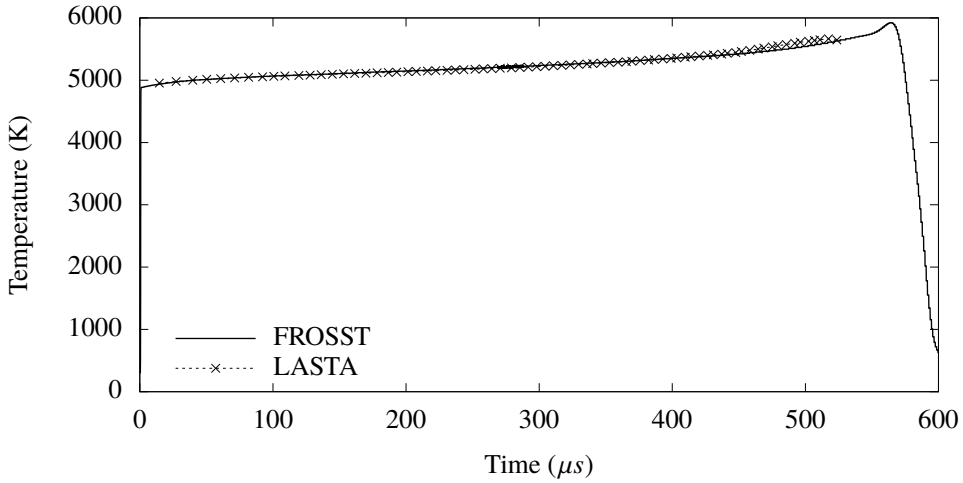

(a) Test gas temperature profiles.

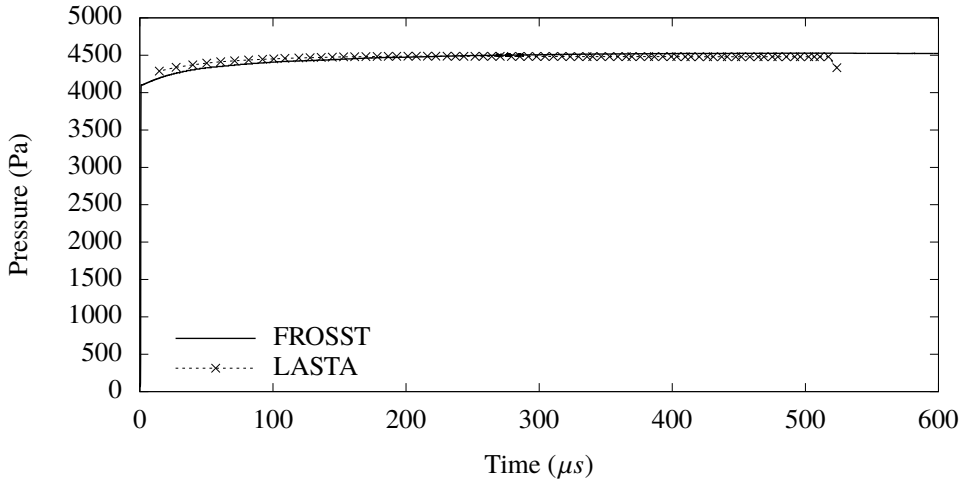

(b) Test gas pressure profiles.

Fig. B1 Shock trajectories and resulting test gas traces in the presence of complex upstream waves.

[6] Kotov, D. V., Yee, H., Panesi, M., Prabhu, D. K., and Wray, A. A., "Computational Challenges for Simulations Related to the NASA Electric Arc Shock Tube (EAST) Experiments," *Journal of Computational Physics*, Vol. 269, 2014, pp. 215 – 233.

[7] Brandis, A., Cruden, B., Prabhu, D., Bose, D., McGilvray, M., Morgan, R., and Morgan, R., "Analysis of Air Radiation Measurements Obtained in the EAST and X2 Shocktube Facilities," *10th AIAA/ASME Joint Thermophysics and Heat Transfer Conference*, American Institute of Aeronautics and Astronautics, 2010. https://doi.org/10.2514/6.2010-4510.

[8] Brandis, A. M., and Cruden, B. A., "Shock Tube Radiation Measurements in Nitrogen," *2018 Joint Thermophysics and Heat Transfer Conference*, American Institute of Aeronautics and Astronautics, 2018. https://doi.org/10.2514/6.2018-3437, URL https://doi.org/10.2514/6.2018-3437.

[9] Mirels, H., "Flow Nonuniformity in Shock Tubes Operating at Maximum Test Times," *Physics of Fluids*, Vol. 9, No. 10, 1966, p. 1907. https://doi.org/10.1063/1.1761542.

[10] Satchell, M., Mare, L. D., and McGilvray, M., "Flow Non-Uniformities Behind Accelerating Shockwaves in Shock Tubes," *AIAA Scitech 2021 Forum*, American Institute of Aeronautics and Astronautics, 2021. https://doi.org/10.2514/6.2021-0649, URL https://doi.org/10.2514/6.2021-0649.

[11] James, C. M., Smith, D. R., McLean, C., Morgan, R. G., Lewis, S. W., Toniato, P., Wei, H., and McIntyre, T. J., "Using Optically Filtered High-Speed Imaging to Characterise Expansion Tube Operating Conditions," *Shock Waves*, Vol. 30, No. 5, 2020, pp. 523–544. https://doi.org/10.1007/s00193-020-00948-x.

[12] Anderson, J., *Hypersonic and High Temperature Gas Dynamics*, American Institute of Aeronautics and Astronautics, Reston, VA, 2000.

[13] Bensassi, K., Brandis, A. M., and Cruden, B. A., "Computational Modelling for Non-equilibrium Shock Tube Flows," *Proceedings of the 32nd International Symposium on Shock Waves (ISSW32 2019)*, Research Publishing Services, 2019. https://doi.org/10.3850/978-981-11-2730-4_0468-cd, URL https://doi.org/10.3850/978-981-11-2730-4_0468-cd.

[14] Jacobs, P. A., "Quasi-One-Dimensional Modeling of a Free-Piston Shock Tunnel," *AIAA Journal*, Vol. 32, No. 1, 1994, pp. 137–145. https://doi.org/10.2514/3.11961.

[15] James, C. M., Gildfind, D. E., Lewis, S. W., Morgan, R. G., and Zander, F., "Implementation of a State-to-State Analytical Framework for the Calculation of Expansion Tube Flow Properties," *Shock Waves*, Vol. 28, No. 2, 2018, pp. 349–377. https://doi.org/10.1007/s00193-017-0763-3.

[16] Priyadarshini, M. S., Munafò, A., Brandis, A. M., Cruden, B. A., and Panesi, M., "One-Dimensional Modeling Methodology for Shock Tubes: Application to the EAST facility," *2018 Joint Thermophysics and Heat Transfer Conference*, American Institute of Aeronautics and Astronautics, 2018. https://doi.org/10.2514/6.2018-4181, URL https://doi.org/10.2514/6.2018-4181.

[17] Gollan, R., and Jacobs, P., "About the Formulation, Verification and Validation of the Hypersonic Flow Solver Eilmer," *International Journal for Numerical Methods in Fluids*, Vol. 73, No. 1, 2013, pp. 19–57. https://doi.org/10.1002/fld.3790, URL https://doi.org/10.1002/fld.3790.

[18] Bensassi, K., and Brandis, A. M., "Time Accurate Simulation of Nonequilibrium Flow Inside the NASA Ames Electric Arc Shock Tube," *AIAA Scitech 2019 Forum*, American Institute of Aeronautics and Astronautics, 2019. https://doi.org/10.2514/6.2019-0798.

[19] Holbeche, T. A., and Spence, D. A., "A Theoretical and Experimental Investigation of Temperature Variation Behind Attenuating Shock Waves," *Proceedings of the Royal Society of London. Series A, Mathematical and Physical Sciences*, Vol. 279, No. 1376, 1964, pp. 111–128. URL http://www.jstor.org/stable/2414836.

[20] Light, G. C., "Test Gas Properties Behind a Decelerating Shock Wave in a Shock Tube," *Physics of Fluids*, Vol. 16, No. 5, 1973, p. 624. https://doi.org/10.1063/1.1694397.

[21] Satchell, M., Glenn, A., Collen, P., Penty-Garaets, R., McGilvray, M., and di Mare, L., "An Analytical Method of Evaluating Nonuniformities in Shock Tube Flows. Part 2: Application," , 2021. Submitted to AIAAJ.

[22] Collen, P. L., Doherty, L., McGilvray, M., Naved, I., Geraets, R. T. P., Hermann, T. A., Morgan, R. G., and Gildfind, D., "Computations of High Enthalpy Shock-waves in Electric Arc Shock-Tube (EAST) at NASA Ames," *57th AIAA Aerospace Sciences Meeting*, American Institute of Aeronautics and Astronautics, 2019. https://doi.org/10.2514/6.2019-1941.

[23] Hooker, W. J., "Testing Time and Contact-Zone Phenomena in Shock-Tube Flows," *Physics of Fluids*, Vol. 4, No. 12, 1961, p. 1451. https://doi.org/10.1063/1.1706243, URL https://doi.org/10.1063/1.1706243.

[24] Mirels, H., "Laminar Boundary Layer Behind a Strong Shock Moving Into Air," *NACA Technical Note D-291*, 1961.

[25] Mirels, H., "Boundary Layer Behind Shock or Thin Expansion Wave Moving Into Stationary Fluid," *NACA TN-3712*, 1956.

[26] McBride, B., and Gordon, S., "Computer program for calculation of complex chemical equilibrium compositions and applications. I: Analysis," *NASA-RP-1311*, Vol. 19, 1996.

[27] McBride, B., and Gordon, S., "Computer program for calculation of complex chemical equilibrium compositions and applications. II: Users Manual and Program Description," *NASA-RP-1311*, Vol. 19, 1996.

[28] Roe, P., "Approximate Riemann solvers, Parameter Vectors, and Difference Schemes," *Journal of Computational Physics*, Vol. 43, No. 2, 1981, pp. 357 – 372. https://doi.org/https://doi.org/10.1016/0021-9991(81)90128-5.

[29] Weilmuenster, K., "An Experimental Investigation of Wall Boundary Layer Transition Reynolds Numbers in an Expansion Tube," *NASA Technical Report NASA-NASA-TN-D-7541, L-9337*, 1974.

[30] Mirels, H., "Shock Tube Test Time Limitation Due to Turbulent Wall Boundary Layer," *AIAA Journal*, Vol. 2, No. 1, 1964, pp. 84–93. https://doi.org/10.2514/3.2218.

[31] Eckert, E. R., "Survey on Heat Transfer at High Speeds," *WADC TR 54-70*, 1962.

[32] Simon, H., Liu, C., and Hartnett, J., "The Eckert Reference Formulation Applied to High-Speed Laminar Boundary Layers of Nitrogen and Carbon Dioxide," *International Journal of Heat and Mass Transfer*, Vol. 10, No. 3, 1967, pp. 406–409. https://doi.org/10.1016/0017-9310(67)90159-7, URL https://doi.org/10.1016/0017-9310(67)90159-7.